Journal of Alloys and Compounds, 195 (1993) 483–490
JALCOM 7512

Magneto-optical imaging of Shubnikov phase

Th. Schuster, M. R. Koblischka and H. Kronmüller

MPI für Metallforschung, Institut für Physik
D-7000 Stuttgart-80, Heisenbergstr.1, F.R.Germany

Abstract

Among the various methods to obtain images of the Shubnikov phase in superconductors the high-resolution Faraday effect enables one to local (spatial resolution of about 0.8 μm) and dynamic observations of domain structures. In this paper the different types of flux penetration into the different kinds of high-T_c samples (sintered materials, single crystals and thin films) are presented. It is found that the obtained domain structures of single crystalline materials depend strongly on the geometry of the samples.
The possibility to local observations allows to study the influence of various microstructures on the pinning behaviour. As a new feature of the high-T_c superconductors, it is shown that in the remanent state vortices of opposite polarity have nucleated at the sample edges. Domain patterns of high energy heavy-ion irradiated high-T_c samples show the advantages of a local determination of the acting volume pinning forces and critical current densities. Using the capability to dynamic observations, flux creep effects can be visualised.

1. Introduction

To observe directly the behaviour of Shubnikov phase in superconductors, many methods are described in the literature and are also applied to high-T_c superconductors [1–6]. Among them, only the high-resolution Faraday effect (HRF) technique combines a high spatial resolution ($\approx$ 0.8 μm) with the possibility to dynamic observations of domain structures. So, the HRF technique enables one to study the influence of microstructure on the pinning behaviour in a direct way.
In this paper, a comparison of flux penetration into various types of high-T_c samples (sintered samples, single crystals and epitaxial thin films) is discussed, and, new features not observed on conventional superconductors are presented. As an application of the HRF technique, local determinations of critical current densities and effective activation energies on partly heavy-ion irradiated $DyBa_2Cu_3O_{7-\delta}$ single crystals are also shown.

2. Faraday effect

The magnetic field distribution of a superconductor in the Shubnikov phase Bis imaged by detecting the rotation of the polarization plane of the linear polarized light within the magneto-optical layer in regions where flux is present in the underlying superconductor. In regions without flux, the light is reflected without rotation of the polarization plane. This light is not able to pass the analyzer which is set in crossed position with respect to the polarizer. In this way, the Shubnikov phase will be imaged as bright domains whereas the Meissner phase remains dark. To achieve an observable rotation angle of the polarized light, several conditions for the thickness of the magneto-optical active layer have to be fulfilled [7, 8]. Observations by means of the HRF technique are possible only in the temperature range 5 K $\leq T \leq$ 20 K. The lower boundary is given by the cryostat used; the upper boundary is imposed by the temperature dependent Verdet constant of the Europium chalcogenides thus leading at high temperatures ($T >$ 20 K) to very low contrasts between Meissner and Shubnikov phase.
For a detailed description of the experimental setup we refer to [8, 9, 10]. All images can be observed directly at the microscope or may be transferred to an image-processing system for analyzing purposes [7]. The external magnetic field is generated by a copper solenoid coil producing a maximum field of 0.5 T or by a small pulsed coil which is mounted directly beneath

0925-8388/93/$06.00

the sample and is cooled down to $T = 5$ K together with the sample. This small coil allows to reach external magnetic fields up to 1.3 T. The length of the pulses is typically 15 ms thus allowing observations of remanent states only with the camera system used.
To calibrate the obtained flux-density profiles in terms of the local flux-density, $B_z(x)$, a comparison between the intensities of the light measured at the superconductor and at a Schott BK 7 glass coated also with the EuSe layer was performed [8]. From these calibrated flux-density profiles, the acting local volume pinning forces, $f_p(x)$, and critical current densities, $j_c(x)$, are obtained [7, 8] using the model described by Friedel et al. [11] in a one-dimensional form:

$$j_c(x) = \frac{1}{\mu_0} \frac{\partial B_z(x)}{\partial x} \tag{1}$$

and

$$f_p(x) = j_c(x) B_z(x) \tag{2}$$

In these equations effects of curved flux-lines are not regarded [12, 13]. In this way, the critical current densities determined from the measured flux density profiles on thin film samples are too low as the current is mostly carried by the undetectable gradient $\partial B_r / \partial z$ (cylindrical coordinates). To solve this problem a numerical calculation method was developed by Theuss *et al.* [13] which reproduces the measurement via the Biot-savart law.

3. Results and discussion

The observation temperature in all experiments shown is $T = 5$ K. The external magnetic field is oriented perpendicular to the sample surface and hence parallel to the *c*-axis of the single crystalline materials.

3.1 Flux penetration in different high-T_c samples

In figs. 1 (a) and (b), domain patterns obtained on a sintered $YBa_2Cu_3O_{7-\delta}$ sample (a – $\mu_0 H_{ext}$ = 273 mT) and on a $DyBa_2Cu_3O_{7-\delta}$ single crystal (b – $\mu_0 H_{ext}$ = 273 mT) are shown. The flux is found to penetrate a sintered sample in two steps [14–16] and only the last step, the penetration of flux into single grains, can be detected magneto-optically. In large grains, a flux front is observed within the grain. Also the orientation of the grains with respect to the external magnetic field can be observed directly. As described in a previous paper, the magneto-optically determined local pinning forces depend reciprocally on the grain size [17]. In contrary to the sintered samples, the single crystal shows the penetration of a flux front into the sample.

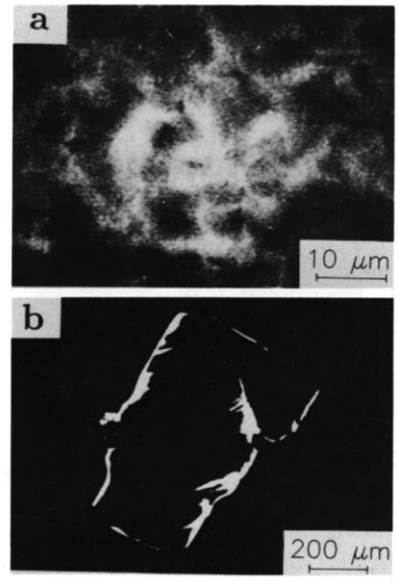

Figure 1. *Observation of flux penetration into a sintered $YBa_2Cu_3O_{7-\delta}$ sample (a – $\mu_0 H_{ext}$ = 273 mT) and into a $YBa_2Cu_3O_{7-\delta}$ single crystal (b – $\mu_0 H_{ext}$ = 246 mT)at $T = 5$ K; the external magnetic field is oriented perpendicular to the sample surface. Clearly visible is the penetration of flux into single superconducting grains in (a) whereas the single crystal (b) shows the penetration of a flux front.*

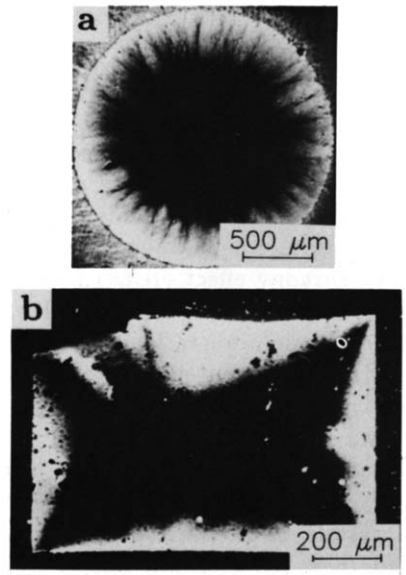

Figure 2. *(a) Observation of flux penetration into an epitaxial thin film of $YBa_2Cu_3O_{7-\delta}$ at $T = 5$ K and $\mu_0 H_{ext}$ = 130 mT. A defect-free homogeneous sample will show a radial symmetric domain pattern. (b) Domain pattern obtained on a rectangular $DyBa_2Cu_3O_{7-\delta}$ single crystal at $T = 5$ K and $\mu_0 H_{ext}$ = 273 mT. The penetration of flux is found to be largest in the middle of the sample edges.*

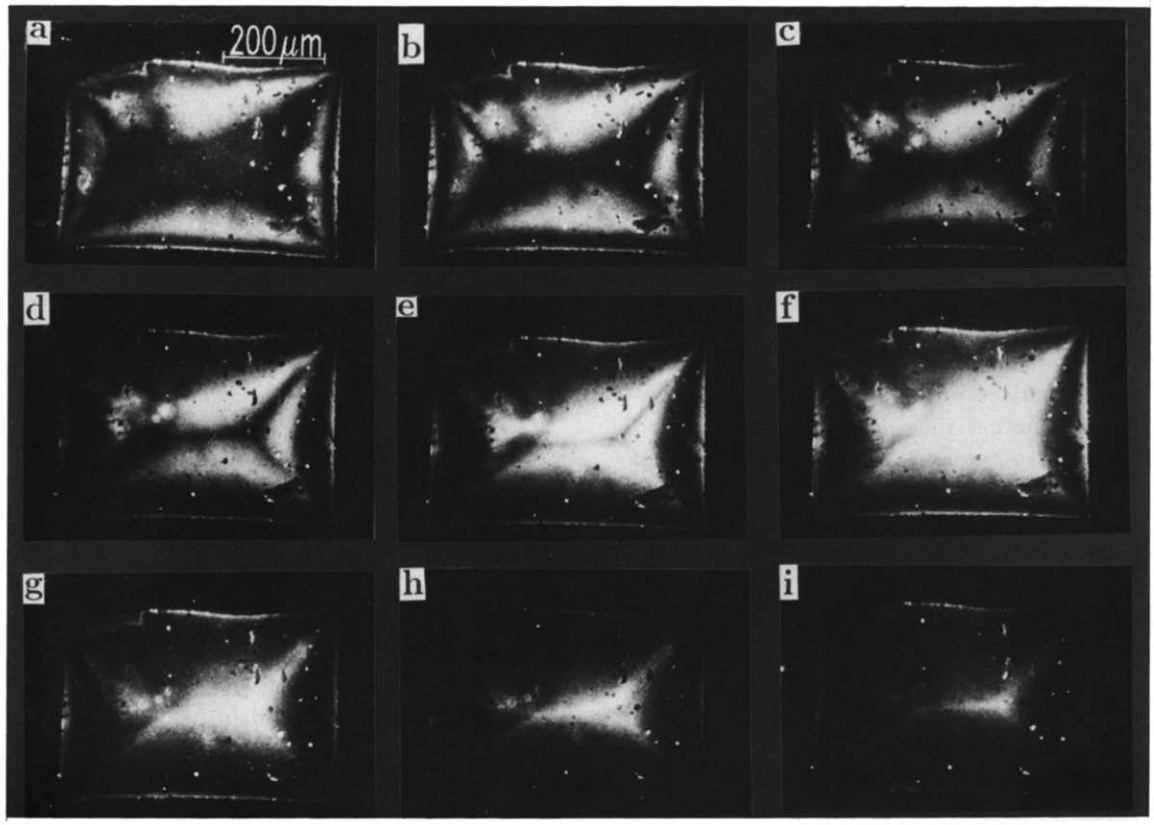

Figure 3: *Domain patterns of a $DyBa_2Cu_3O_{7-\delta}$ single crystal with a nearly rectangular shape in the remanent state using the pulse technique; the temperature is $T = 5$ K. (a) $\mu_0 H_r = 210$ mT. (b) $\mu_0 H_r = 260$ mT. (c) $\mu_0 H_r = 300$ mT. (d) $\mu_0 H_r = 340$ mT. (e) $\mu_0 H_r = 380$ mT. The white arrows point at the newly entered domains of flux lines with opposite polarity. (f) $\mu_0 H_r = 430$ mT. The full penetration state ($\mu_0 H^*$) is reached and the Meissner phase has vanished completely. (g) $\mu_0 H_r = 680$ mT. (h) $\mu_0 H_r = 1020$ mT. The intensity of the Shubnikov phase decreases. (i) $\mu_0 H_r = 1300$ mT.*

3.2 Geometry dependence of the domain patterns

The domain patterns obtained on single crystalline materials are found to depend strongly on the sample geometry [18, 19]. This is shown in figs. 2 (a) and (b) for a circular patterned $YBa_2Cu_3O_{7-\delta}$ thin film (fig. 2 (a)) and for a nearly rectangular $DyBa_2Cu_3O_{7-\delta}$ single crystal (fig. 2 (b)). In a sample with a nearly rectangular shape the penetration is found to be largest in the middle of each sample edge and no penetration starting from the corners is detected. This behaviour was also found on conventional superconductors like thin niobium foils [20]. On epitaxial thin films also the penetration of flux as a flux front is found if the sample is homogeneous and contains no disturbations like small cracks or improperties in the substrate. Such defects will be detected immediately using the HRF technique; so the HRF technique could be applied to control the homogeneity of superconducting devices.

3.3. Nucleation of vortices with opposite polarity

Due to the large demagnetizing factors of the samples investigated here and the small lower critical fields, in high-T_c samples the nucleation of vortices of opposite polarity as the pinned vortices is observed directly [21, 22]. In figs. 3 (a) – (i), remanent states of a nearly rectangular, twin-free $DyBa_2Cu_3O_{7-\delta}$ single crystal are shown using the pulse technique. Fig. 3 (a) shows the crystal after applying an external magnetic field of 210 mT; in the following we will use the abbreviation $\mu_0 H_r$ to characterize the remanent states. In this image, we have now the following multi-domain pattern (from the sample edge to the centre of the sample) formed by: (1) a domain located directly at the sample edges consisting of newly entered vortices of opposite polarity (called 'negative' direction) with respect to the pinned vortices; (2) the so-called annihilation zone where $B_z = 0$ mT; (3) the domain of pinned vortices with 'positive' direction; (4) the Meissner phase as the crystal could not be filled completely

with flux at this relatively small external magnetic field. In previous papers [21, 22] it was shown that these 'negative' vortices are generated by the stray fields of the pinned vortices. Due to the large demagnetizing factors of the samples investigated here the stray fields are large enough to nucleate new visible vortices of opposite polarity.

In the following images, figs. 3 (b) – (e), the external magnetic field is raised stepwise until in fig. 3 (f) the full penetration state, $\mu_0 H^*$, is reached. On further raising the external field in figs. 3 (g) – (i), the measured intensity of the flux begins to decrease. The domain of vortices with opposite polarity behaves in the same manner thus indicating the coupled behaviour of the two domains. In the case of external fields larger than $\mu_0 H^*$, more flux lines enter the crystal causing larger stray fields which generate a larger amount of vortices of opposite polarity. So, there is an increasing process of annihilation of vortices of opposite sign thus leading to a large zone with a small flux density and to vanishing pinned vortices.

3.4. Flux creep effects

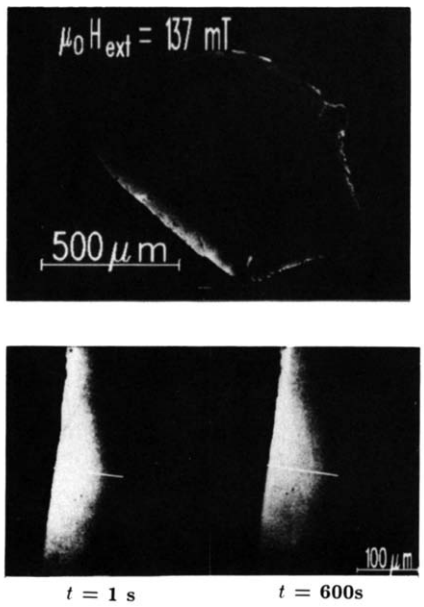

Figure 4. *(a) Domain pattern of a $DyBa_2Cu_3O_{7-\delta}$ single crystal at $T = 5$ K, $\mu_0 H_{ext} = 137$ mT. The time-dependent observations are carried out on the lower sample edge. (b) Undisturbed region of the same crystal shown with higher magnification, $t = 1$ s. (c) Same region as in (b), but after $t = 600$ s. Clearly visible is the relaxation of the domain into the Meissner region.*

Fig. 4 (a) shows a $DyBa_2Cu_3O_{7-\delta}$ single crystal at an external field of $\mu_0 H_{ext} = 137$ mT. On the lower sample edge, a time-dependent observation of the domain patterns is performed using a higher magnification. This observation is presented in figs. 4 (b) and (c) at $t = 1$ s and $t = 600$ s. The deeper penetration of flux into the Meissner region is obvious. From these observations, we determine the amount of flux in a given region by integrating the flux density profiles. Using these data, the effective activation energies for flux creep can be estimated using the model of Beasley *et al.* [23] and of Hagen and Griessen [24]

$$S = -\left.\frac{d\Phi}{\Phi(t_{\text{start}}) \cdot d\ln(t)}\right|_{t=t_{\text{start}}} = -\left(\frac{\pm 1}{U/k_B \cdot T \pm \ln(t_{start}/\tau_0)}\right) \quad . \qquad (3)$$

Here S denotes the creep rate, τ_0 the relaxation time, Φ the flux in the sample or in the chosen region, t_{start} is the starting time of the experiment and k_B the Boltzmann constant. The plus sign in eq. (3) is valid for an increasing applied field before starting the relaxation experiment under a constant field, the negative sign holds for a relaxation experiment after decreasing the external magnetic field and in the remanent state. τ_0 is calculated from the experimental data using the description given by Schnack *et al.* [25].

At a temperature of $T = 5$ K and external fields in the range of 100 – 300 mT, the magneto-optically determined activation energies of $YBa_2Cu_3O_{7-\delta}$, $DyBa_2Cu_3O_{7-\delta}$ and Bi-2212 single crystals lay in the range of 10 – 30 meV [26].

3.5. Heavy-ion irradiated samples

As an example for application of the HRF technique observations of domain patterns on heavy-ion irradiated high-T_c samples is shown. The $DyBa_2Cu_3O_{7-\delta}$ single crystal was irradiated with 0.5 GeV iodine ions with a fluence of $\varphi t = 9.0 \times 10^{10}$ ions/cm^2. The irradiation was carried out at the low temperature facility of VICKSI at the Hahn-Meitner institute, Berlin. This kind of irradiation produces columnar tracks with a diameter of ≈ 10 nm in the target material. These columnar tracks are found to be very effective pinning centres in previous papers [27–31].

To allow a simultaneous observation of irradiated and unirradiated regions under the same experimental conditions, only a part of the crystal was exposed to the irradiation while covering the other part with

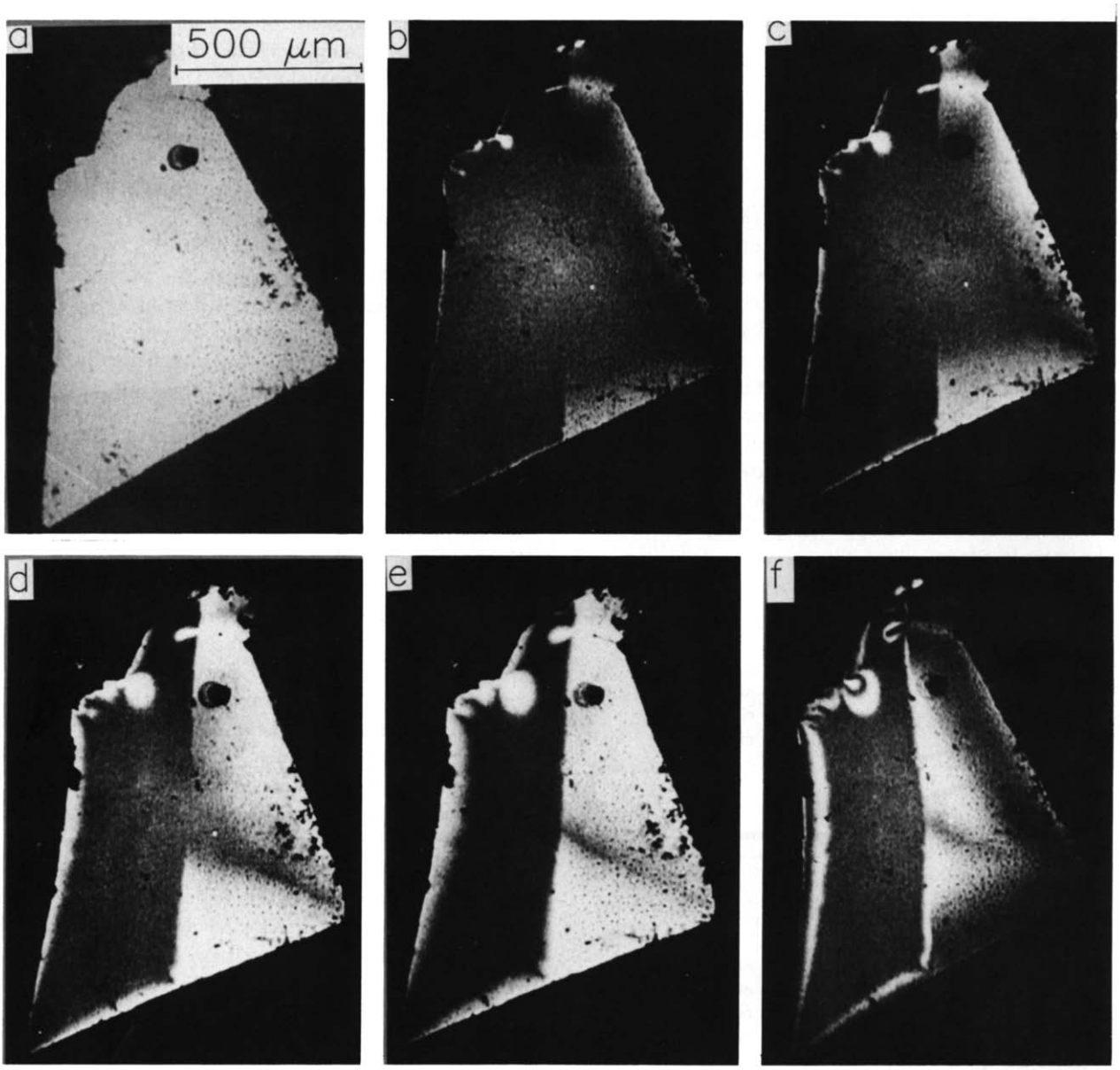

Figure 5: *Domain patterns at $T = 5$ K of a $DyBa_2Cu_3O_{7-\delta}$ single crystal irradiated with 0.5 GeV ^{127}I-ions ($\varphi t = 9.0 \times 10^{10}$ ions/cm^2) as an overview measurement. Only the left half of the crystal was exposed to the irradiation. (a) The $DyBa_2Cu_3O_{7-\delta}$ single crystal cooled down to $T = 5$ K. The photograph is taken with polarizer and analyzer set in uncrossed position ('bright image'). The right half of the crystal was covered with a copper shield during the irradiation. (b) Domain pattern obtained at an external field $\mu_0 H_{ext} = 171$ mT. Clearly visible is the border between the irradiated and the non-irradiated region, causing a deeper penetration of flux along this border. (c) $\mu_0 H_{ext} = 256$ mT. (d) Domain pattern obtained at $\mu_0 H_{ext} = 341$ mT. (e) $\mu_0 H_{ext} = 512$ mT. The unirradiated part of the crystal is filled completely with flux. Also, a penetration of flux starting at the border into the irradiated region is found. From these images one can clearly see that the critical currents, $j_c(\varphi t)$, in the irradiated half of the crystal are much larger than in the unirradiated part, $j_c(0)$. (f) Corresponding remanent state ($\mu_0 H_{ext} = 0$ mT) to fig. 5 (e). At the sample edges, vortices with opposite sign to the pinned vortices have nucleated.*

an absorber. Figs. 5 (a) – (f) show an overview measurement using a small magnification at a temperature $T = 5$ K. In fig. 5 (a), the crystal is shown with analyzer and polarizer set in uncrossed position for comparison with the following images. In fig. 5 (b), an external magnetic field of $\mu_0 H_{ext} = 171$ mT is applied to the sample. Clearly visible are the differences between the irradiated part (left) and the unirradiated part (right) of the crystal. In figs. 5 (c) to (e), the external magnetic field is raised stepwise from $\mu_0 H_{ext} = 256$ mT (c), $\mu_0 H_{ext} = 341$ mT (d) to $\mu_0 H_{ext} = 512$ mT (e). In fig. 5 (e), the unirradiated part of the crystal is filled up completely with flux whereas in the irradiated part a large amount of Meissner phase resides. From these images one can clearly see that the critical currents in the irradiated half of the crystal are much larger than in the unirradiated part. Fig. 5 f presents the corresponding remanent state to fig. 5 (e). Again, flux lines of opposite polarity are found at the sample edges.

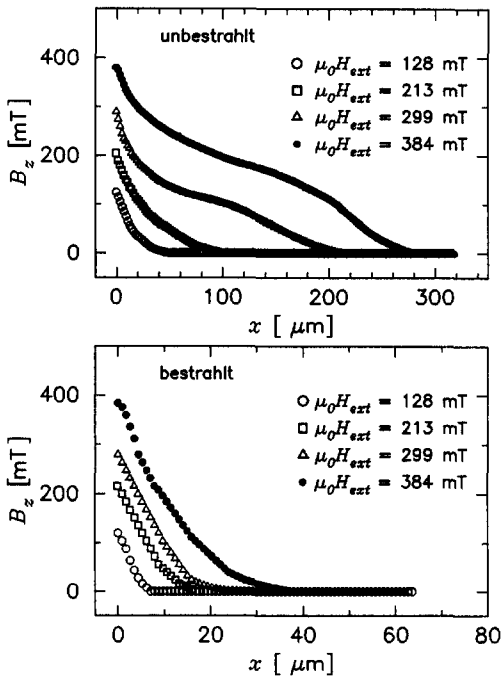

Figure 6. *Flux density profiles read on the iodine-irradiated $DyBa_2Cu_3O_{7-\delta}$ single crystal shown in fig. 5. Flux density profiles of the non-irradiated area are presented in the upper plot at various applied external fields and in the lower plot the flux density profiles of the irradiated area are shown. The deeper flux penetration in the unirradiated area of the crystal is obvious; please note the different length scales of the plots.*

The domain patterns of the heavy-ion irradiated $DyBa_2Cu_3O_{7-\delta}$ single crystal show also the typical, geometry-dependent shape of the domains in both parts of the crystal. Along the border between the two regions, however, the flux penetrates deeper into the unirradiated part of the crystal thus leading to a disturbation of the domain patterns which would have been established in a rectangular $DyBa_2Cu_3O_{7-\delta}$ single crystal as shown in fig. 2 (a). The deeper flux penetration along the border is due to the differences of the critical current densities flowing along this border. Both the irradiated and the unirradiated part of the crystal are found to act magnetically independent from each other. With these assumptions and knowing the geometry-dependence of the domain patterns as shown in fig. 2 (a) and (b), it is possible to reconstruct the domain patterns of a complete irradiated or unirradiated crystal from the domain structures obtained from our partly irradiated samples.

Fig. 6 shows the flux density profiles obtained on the non-irradiated part (upper plot) and on the irradiated region (lower plot). The profiles are shown at the same applied external magnetic fields but at different length scales (unirradiated part 0 – 320 μm, irradiated part 0 – 60 μm). The profiles of the irradiated region show the typical linear or hyperbolic behaviour of high-T_c single crystals. The flux density profiles found have a nearly linear shape, only the profiles obtained at the largest fields in the unirradiated area reflect the influence of the flux penetrating from the other side of the crystal. The penetration depth of the flux in the unirradiated region is deeper by a factor of 8 than in the irradiated area. Using such flux density profiles, the local critical current densities are obtained using eq. (1).

Our results on iodine-irradiated $DyBa_2Cu_3O_{7-\delta}$ single crystals irradiated at various fluences $\varphi t = 7.6 \times 10^{10}$ ions/cm^2 (sample D1) $\varphi t = 9.0 \times 10^{10}$ ions/cm^2 (sample D2) and $\varphi t = 30.0 \times 10^{10}$ ions/cm^2 (sample D3) are summarized in Table 1. In the field range investigated here, it is found that the dependence of the critical current density on the external magnetic field is nearly constant. The critical current densities of the unirradiated areas, $j_c(0)$, are shown together with the critical current densities of the irradiated regions, $j_c(\varphi t)$, and with the relative enhancement, $j_c(\varphi t)/j_c(0)$. This is to allow a comparison of the critical current densities despite of a scatter in the sample quality. At all fluences an enhancement of j_c is found as j_c in sample D1 is enhanced by a factor of 15, in sample D2 by a factor of 8.2 and in sample D3, irradiated at a fluence $\varphi t = 30.0 \times 10^{10}$ ions/cm^2, by

sample	φt [10^{10} ions/cm^2]	$j_c(0)$ [10^9 A/m^2]	$j_c(\varphi t)$ [10^9 A/m^2]	$j_c(\varphi t)/j_c(0)$
D1	7.6	0.7	11	15.2
D2	9.0	1.5	13	8.3
D3	30.0	6.0	200	33.0

Table 1: *Magneto-optically determined critical current densities, j_c, at $T = 5$ K in iodine-irradiated $DyBa_2Cu_3O_{7-\delta}$ single crystals. $j_c(0)$ is taken from the unirradiated part of the sample, $j_c(\varphi t)$ from the irradiated part of the sample.*

a factor of 33.
The flux creep experiments also performed on iodine-irradiated $DyBa_2Cu_3O_{7-\delta}$ single crystals, however, do not show any significant irradiation-induced change as on crystal D1 the activation energy of the unirradiated region, $U(0)$, is determined to 22 meV and for the irradiated region, $U(\varphi t)$, is found to be 24 meV. The difference between both values is smaller than the experimental error of $\pm$ 3 meV. Similar results are obtained on the other crystals [31].
As one would expect an activation energy in the range of 1 eV to move an Abrikosov flux line out of a columnar track, these results suggest that also in the 1-2-3 system the vortices have to be described as so-called pancake vortices [32] like in the case of the Bi-2212 superconductors [28, 30].

4. Conclusions

In the present paper we have demonstrated the advantages of a local observation of Shubnikov phase in superconductors. The HRF method enables one to study the influence of microstructure on the pinning behaviour in a direct way. It is shown that the flux penetration in sintered samples is totally different from single crystalline materials like single crystals or epitaxial thin films, as the flux penetrates into single superconducting grains. The domain patterns obtained on single crystalline samples are found to depend strongly on the sample geometry. The existence of domains with opposite polarity in the remanent states of all high-T_c superconductors was not observed on conventional superconductors.
Using the HRF technique also dynamic processes can be observed as shown with the direct observations of flux creep effects. The magneto-optically determined activation energies for flux creep are found to be very small, typical values of $YBa_2Cu_3O_{7-\delta}$, $DyBa_2Cu_3O_{7-\delta}$ and Bi-2212 single crystals lay in the range of 10 – 30 meV ($T = 5$ K, $\mu_0 H_{ext} = 150$ mT).
The observations of domain patterns of partly heavy-ion irradiated single crystals demonstrate the advantages of the local determinations of critical current densities via the HRF technique as irradiated and unirradiated regions can be observed simultaneously under the same experimental conditions. Columnar tracks as induced by 0.5 GeV iodine irradiation are found to be very effective pinning centres, however, the effective activation energies for flux creep remain unchanged.

Acknowledgements

The authors want to thank U. Eßmann, E. H. Brandt, H. Kuhn, H. Theuss, A. Forkl, B. Ludescher, P. Keppler, E. Lutkat (MPI Stuttgart), M. Leghissa, M. Kraus, Prof. G. Saemann-Ischenko (University of Erlangen) and Prof. R. Griessen (Free University Amsterdam) for assistance and helpful discussions. The authors are indebted to S. Klaumünzer (HMI Berlin) for the irradiation experiments. Financial support by the Bundesministerium für Forschung und Technologie is gratefully acknowledged.

References

1 H. Träuble and U. Eßmann, *Phys. stat. sol.* **25** (1968) 395.

2 H. Kirchner, *Phys. Lett. A* **30** (1969) 437.

3 A. Ourmazd, J. A. Rentschler, W. J. Skocpol and D. W. Johnson jr., *Phys. Rev. B* **36** (1987) 8914.

4 N. Moser, M. R. Koblischka, B. Gegenheimer and H. Kronmüller, *Physica C* **159** (1989) 117.

5 M. V. Indenbom, N. N. Koleshnikov, M. P. Kulakov, I. G. Naumeko, V. I. Nikitenko, A. A. Polanskii, N. F. Vershinin and V. K. Vlasko-Vlasov, *Physica C* **166** (1990) 486.

6 E. Batalla, E. G. Zwartz, R. Goudreault and L. S. Wright, *Rev. Sci. Instrum.* **61** (1990) 2194.

7 M. R. Koblischka, N. Moser, B. Gegenheimer and H. Kronmüller, *Physica C* **166** (1990) 36.

8 Th. Schuster, M. R. Koblischka, N. Moser, B. Ludescher and H. Kronmüller, *Cryogenics* **31** (1991) 811.

9 K.-H. Greubel, E. Gmelin, N. Moser, Ch. Mensing and L. Walz, *Cryogenics* **30** (suppl.) (1990) 457.

10 B. Ludescher, Th. Schuster, M. R. Koblischka, N. Moser and H. Kronmüller, *Laser und Optoelektronik* **23(4)** (1991) 54.

11 J. Friedel, P. G. deGennes and H. Matricon, *Appl. Phys. Lett.* **2** (1963) 119.

12 L. T. Baczewski, K. Piotrowski, R. Szymczak and A. P. Malozemoff, *Physica C* **175** (1991) 363.

13 H. Theuss, A. Forkl and H. Kronmüller, *Physica C* **190** (1992) 345.

14 J. R. Clem, *Physica C* **153-155** (1988) 50.

15 M. Kohl, M. Odehnal, M. Plitovič and S. Safrata, *J. Low Temp. Phys.* **74** (1989) 503.

16 Th. Schuster, M. R. Koblischka, T. Reininger, B. Ludescher, R. Henes and H. Kronmüller, *Supercond. Sci. Tech.* **5** (1992) 614.

17 N. Moser, M. R. Koblischka and H. Kronmüller, *J. Less Com. Met.* **164–165** (1990) 1308.

18 P. Brüll, D. Kirchgässner and P. Leiderer, *Physica C* **182** (1991) 359.

19 Th. Schuster, M. R. Koblischka, H. Kuhn, B. Ludescher, M. Leghissa, M. Lippert and H. Kronmüller, *Physica C* **196** (1992) 373.

20 R. P. Hübener, V. A. Rowe and R. T. Kampwirth, *Proccedings of the 12th Int. Conf. on Low. Temp. Phys., Kyoto, Japan*, ed. by E. Kanda (1970) 467.

21 Th. Schuster, M. R. Koblischka, N. Moser and H. Kronmüller, *Physica C* **179** (1991) 269.

22 Th. Schuster, M. R. Koblischka, B. Ludescher and H. Kronmüller, *J. Appl. Phys.* **72** (1992) 1478.

23 M. R. Beasley, R. Labusch and W. W. Webb, *Phys. Rev.* **8** (1969) 682.

24 C. W. Hagen and R. Griessen, *Phys. Rev. Lett.* **62** (1989) 2657.

25 H. G. Schnack, R. Griessen, J. G. Lensink, C. J. van der Beek and P. H. Kes, *Physica C* **197** (1992) 337.

26 M. R. Koblischka, Th. Schuster, B. Ludescher and H. Kronmüller, *Physica C* **190** (1992) 557.

27 L. Civale, A. D. Marwick, T. K. Worthington, M. A. Kirk, J. A. Thompson, L. Krusin-Elbaum, Y. Sun, J. R. Clem and F. Holtzberg, *Phys. Rev. Lett.* **67** (1991) 648.

28 W. Gerhäuser, G. Ries, H.-W. Neumüller, W. Schmidt, O. Eibl, G. Saemann-Ischenko and S. Klaumünzer, *Phys. Rev. Lett.* **68** (1992) 879.

29 M. Leghissa, Th. Schuster, W. Gerhäuser, S. Klaumünzer, M. R. Koblischka, H. Kronmüller, H. Kuhn, H.-W. Neumüller and G. Saemann-Ischenko, *Europhysics Lett.* **19** (1992) 323.

30 Th. Schuster, M. R. Koblischka, H. Kuhn, H. Kronmüller, M. Leghissa, W. Gerhäuser, G. Saemann-Ischenko, H.-W. Neumüller and S. Klaumünzer, *Phys. Rev. B* **46** (1992) 8496.

31 Th. Schuster, M. Leghissa, M. R. Koblischka, H. Kuhn, M. Kraus, H. Kronmüller and G. Saemann-Ischenko, *Physica C* **203** (1992) 203.

32 J. R. Clem, *Phys. Rev. B* **43** (1991) 7837.